ROYAL SOCIETY
OF CHEMISTRY

PAPER

Check for updates

Intermediate phase modulation and defect passivation to stabilize the photoactive phase of formamidinium-based perovskites for air-ambient device fabrication

Nitin Kumar Bansal, [ID] [a] Jinyoung Kim, [ID] [b] Gyu Min Kim [ID] *[b] and Trilok Singh [ID] *[a]

Achieving stable and efficient formamidinium (FA)-rich perovskite solar cells (PSCs) in air-ambient conditions remains a critical challenge. In this work, we demonstrate an antisolvent engineering approach for the triple co-solvent system of perovskite formation using n-heptylamine (n-HA) to stabilize the photoactive α-FAPb(I$_x$Br$_{1-x}$)$_3$ phase. By incorporating n-HA into the antisolvent process, we mitigate moisture-induced degradation and achieve superior film morphology. n-HA helps to repel moisture and DMSO-based intermolecular adducts and convert the perovskite into a photoactive black phase even prior to annealing. The Lewis base functional group of n-HA significantly passivated the grain boundaries, resulting in the mitigation of halide vacancy and uncoordinated lead in the perovskite film. The resulting perovskite films exhibit enhanced phase stability, reduced defect density, and improved grain growth and film morphology. The devices fabricated using these films achieve a significant power conversion efficiency (PCE) of 22.56% with minimal hysteresis and excellent stability, highlighting the potential of this strategy for scalable air-ambient PSC fabrication.

1. Introduction

The remarkable rise of organometal halide perovskites as a groundbreaking class of light absorbers for photovoltaic (PV) applications has revolutionized the next-generation thin-film solar-cell landscape.[1] With power conversion efficiencies (PCEs) reaching 27% for single-junction cells and 34.85% for two-terminal perovskite-silicon tandem cells, perovskite solar cells (PSCs) now outperform traditional technologies.[2] This exceptional performance, coupled with the low-cost, solution-based fabrication process, has sparked global efforts to harness the potential of perovskite materials in innovative PV technologies.[3–6] Despite these advances, the commercialization of PSCs faces critical challenges, particularly due to their sensitivity to environmental factors such as humidity, oxygen, and solvent residuals.[7] These environmental interactions significantly constrain their fabrication conditions, often necessitating inert environments with precise humidity and oxygen control, which impose high costs.[8] The fabrication of efficient PSCs under humid ambient conditions presents a significant challenge due to the intrinsic instability of

perovskite materials in such environments.[9] Notably, most high-performance PSCs reported to date originate from lab-scale, small-area devices typically fabricated *via* spin-coating under controlled inert atmospheres, such as nitrogen or argon.[10] While spin-coating within a glovebox ensures operational simplicity and reliable reproducibility, it falls short in terms of scalability for mass production. In contrast, ambient air processing has emerged as a pivotal advancement, bridging the gap between laboratory-scale fabrication and industrial-scale manufacturing of PSCs.[11]

Efforts to overcome these challenges have focused on ambient fabrication strategies to achieve high-efficiency PSCs under practical environmental conditions. In ambient air, moisture interacts with perovskite precursors, causing uncontrollable crystallization and leading to films with rough surfaces, pinholes, and defects.[12] Halide vacancies and uncoordinated metallic groups also diminish the device performance parameters.[13,14] These challenges are especially severe for formamidinium (FA)-based perovskites. Although the FA-based perovskites offer superior stability and a narrower bandgap compared with methylammonium lead iodide (MAPbI$_3$), they struggle to maintain the photoactive black α-FAPbI$_3$ phase under humid conditions.[15] Instead, these films often transform into the photoinactive yellow δ-FAPbI$_3$ phase, severely reducing their performance and stability.

To address these limitations, researchers have explored multiple approaches, including optimized precursor chemistries, solvent engineering, grain boundary passivation, and controlled crystallization techniques.[16–18] For example, the

[a] *Semiconductor Thin Film and Emerging Photovoltaic Laboratory, Department of Energy Science and Engineering, Indian Institute of Technology Delhi, Hauz Khas, New Delhi 110016, India. E-mail: trilok.singh@dese.iitd.ac.in*

[b] *Department of Chemical Engineering, Hankyong National University, 67 Seokjeong-dong, Anseong, Gyeonggi-do 17579, South Korea. E-mail: gyumin@hknu.ac.kr*

incorporation of hydrophobic additives or ionic liquid solvents has been shown to mitigate the moisture effects and stabilize the perovskite phase.[19–21] Substrate heating and antisolvent engineering further aid in tuning crystallization kinetics and improving film quality under ambient conditions. Further, antisolvent engineering has emerged as a crucial strategy for controlling the crystallization dynamics of perovskite films, enabling the formation of uniform, high-quality layers with enhanced optoelectronic properties.[22] By carefully selecting and applying an appropriate antisolvent during the spin-coating process, rapid supersaturation is induced, promoting dense grain formation and suppressing defect states.[23] This technique has been widely adopted to improve film morphology, enhance device performance, and boost the reproducibility of PSCs fabricated under controlled conditions. However, these methods often lack reproducibility and require further refinement to stabilize the α-FAPbI$_3$ phase while achieving smooth, pinhole-free films in humid environments.[24]

Here, we present the application of the liquid long-chain molecule n-heptylamine (n-HA) in FA-rich perovskite films using anti-solvent engineering. As a novel feature of the work, we incorporated a triple-co-solvent system for device fabrication with n-HA in different antisolvents. Hydrophobic n-HA has the ability to lessen the impact of moisture on the perovskite during its formation. This results in intermolecular substitution with the detrimental moisture-induced DMSO-based adduct, which helps in the formation of α-FAPb(I$_x$Br$_{1-x}$)$_3$ at room temperature while retaining the black phase. XRD of the un-annealed film confirms the presence of a photoactive phase even at room temperature. Additionally, the perovskite grain size is substantially enhanced with more uniform grain size distribution, and the n-HA at the grain borders lowers the defect density. Improved morphology is confirmed by SEM and AFM analysis. To check the efficacy of the idea, we tried three different antisolvents, namely chlorobenzene (CB), isopropanol (IPA), and ethyl acetate (ET). The technology employing the optimized FA-based perovskite film, fabricated under controlled relative humidity (RH) conditions of 20% to 30%, results in devices achieving a champion PCE of 22.56%, with minimal hysteresis and excellent reproducibility for nHA + CB-based devices. However, additional anti-solvent combinations also resulted in improved performance. This work provides valuable insights into the interplay between anti-solvent engineering and environmental factors, offering a pathway toward the scalable production of efficient and stable PSCs in ambient air.

2. Raw materials, device fabrication process, and characterizations

2.1 Reagents and materials

The indium-doped tin oxide (ITO) substrates were procured from Greatcell Solar. A 15% SnO$_2$ colloidal solution dispersed in deionized water was supplied by Alfa Aesar. Sigma-Aldrich provided various chemicals, including Hellmanex soap, spiro-OMeTAD, lithium fluoride (LiF), and methylammonium chloride (MACl). Key precursors for the perovskite layer were sourced from Tokyo Chemical Industry (TCI), including formamidinium iodide (FAI), lead bromide (PbBr$_2$), and methylammonium iodide (MAI), all with 99.95% purity, as well as lead iodide (PbI$_2$) with 99.98% purity. TCI also supplied lithium bis(trifluoromethanesulfonyl)imide (Li-TFSI), n-heptylamine (n-HA), and 4-tert-butylpyridine (t-BP), all with a purity of over 98%. Solvents such as N,N-dimethylformamide (DMF), acetonitrile (ACN), dimethyl sulfoxide (DMSO), and chlorobenzene (CB) were sourced from Merck, each with a purity of over 99%. Additionally, acetone, N-methyl-2-pyrrolidone (NMP), and isopropanol (IPA), each with a purity of more than 99%, were purchased from Thermo Scientific. Gold (Au) wire with a purity of over 99.8% was obtained from SK-Novel Materials.

All chemicals were used as received from the respective suppliers and used without any additional purification.

2.2 Device fabrication process

The fabrication of PSCs and thin films was carried out under ambient air conditions with controlled humidity. The ITO substrates underwent a rigorous cleaning procedure before further processing. These were ultrasonicated for 20 minutes in each soap solution, DI, acetone, and IPA, respectively. Following the cleaning steps, the substrates were treated with UV-ozone for 15 minutes to enhance the surface properties prior to the deposition of the electron transport layer (ETL). A 15% SnO$_2$ colloidal solution in deionized water was diluted to a concentration of 2.20%. The diluted solution was spin-coated onto the cleaned ITO substrates at 2500 rpm for 40 seconds. After the spin-coating process, the substrates were annealed at 160 °C for 30 minutes to ensure proper film formation and adhesion. A perovskite solution was formed by dissolving PbI$_2$ (572.14 mg), FAI (216.64 mg), MACl (20.3 mg), MAI (4.25 mg), and PbBr$_2$ (6.95 mg) in DMF:NMP:DMSO (4:0.05:0.95). The above solution was deposited on the SnO$_2$ coated substrate in two steps. The solution was spin-coated at a speed of 1200 rpm for a duration of 5 seconds, followed by an increase to 3500 rpm for 30 seconds. This was succeeded by the application of anti-solvent, which commenced at the 15-second mark of the later step. In the process of anti-solvent engineering, 3 μL of nHA configurable liquid was mixed in 1 mL of various anti-solvents, followed by sonication for several minutes. 100 μL of the above mixture was used as an anti-solvent. The coated substrates were then annealed at 155 °C for 20 minutes. A previously described procedure was employed to prepare a solution for the deposition of the hole transport layer (HTL).[25] The chemical solution was deposited on the perovskite film by spin-coating at a rotational speed of 2500 rpm for 20 seconds. A gold layer measuring 60–65 nm was deposited on the HTL utilising a thermal evaporator, while maintaining a device area of 0.0256 cm^2 through the use of a shadow mask. Electron-only devices were prepared by depositing LiF and Au layers using a thermal evaporation system, while the remaining layers were fabricated according to the procedure described earlier. Commercial LiF powder was used without further treatment, and a film with a thickness of approximately 30 nm was deposited under a chamber pressure below 10^{-5} mbar.

2.3 Characterization techniques

The X-ray diffraction (XRD) patterns were recorded using a Rigaku Miniflex 600 diffractometer. Field-emission scanning electron microscopy (FE-SEM, Hitachi SU-8600) was employed for surface and cross-sectional imaging of the perovskite films. Topographical analysis was performed using an Oxford Instruments (MFP-3D Origin+) atomic force microscope (AFM). Steady-state and time-resolved photoluminescence (SS-PL and TR-PL) spectra were obtained using an Edinburgh Instruments FLS-1000 spectrometer. PL mapping was performed over a 50×50 μm^2 scan area using a Witech Alpha 300R imaging microscope with a 532 nm excitation laser. UV-Visible absorption spectra were recorded using a Shimadzu UV-Vis 3600i Plus spectrometer. Fourier-transform infrared (FTIR) spectra were captured using a JASCO FT/IR-6X instrument. X-ray photoelectron spectroscopy (XPS) analysis was performed using an AXIS Supra system from Kratos Analytical Ltd.

Current–voltage (J–V) measurements were carried out using an Ossila solar cell testing kit (T2003B3-G2009A1) with a PECELL L01 solar simulator (AM 1.5G simulated sunlight spectrum). The incident photon-to-electron conversion efficiency (IPCE) was measured with a McScience K3100 system. Dark J–V measurements were performed over a voltage range of -1.2 V to 1.2 V at a scan rate of 100 mV s^{-1}. For stability studies, unencapsulated devices were stored in the dark under controlled humidity conditions ($20\% \pm 10\%$ RH).

3. Results and discussion

Planar PSCs were fabricated with the device architecture ITO/SnO$_2$/FAPb(I$_x$Br$_{1-x}$)$_3$/spiro-OMeTAD/Au (Fig. 1a). A small quantity of *n*-HA was introduced into the anti-solvent to regulate the intermediate phase formation and enhance grain growth, thereby improving the PCE and stability of the PSCs processed under air-ambient conditions, as illustrated in Fig. 1b. *n*-HA is a linear aliphatic primary amine with a seven-carbon alkyl chain (CH$_3$–(CH$_2$)$_6$–NH$_2$), where the terminal amine group can coordinate with Pb^{2+} ions, while the hydrophobic alkyl chain provides steric hindrance and moisture resistance (Fig. S1). Furthermore, the feasibility and versatility of this approach were assessed by introducing *n*-HA into various anti-solvents, *i.e.*, CB, IPA, and EA. Systematic optimization revealed that a concentration of 3 μL mL^{-1} *n*-HA in CB yielded the most favorable performance in this study. The selection of the anti-solvent and the optimization of its concentration were conducted based on top-view SEM analysis and corresponding device performance data (Fig. S2–S4). This systematic approach ensured the formation of high-quality perovskite films with improved morphology, leading to enhanced photovoltaic performance. Subsequent characterizations and analyses were conducted by comparing the pristine devices with those incorporating the optimized *n*-HA concentration.

3.1 Evolution of phase stabilization

Controlling crystallization and phase stabilization during ambient-air processing of perovskite films remains highly challenging due to the detrimental effects of oxygen and moisture. To address these issues, we incorporated a hydrophobic Lewis base compound, *n*-HA, into the anti-solvent during the film formation process.[26] The presence of *n*-HA played a critical role in regulating the moisture-induced DMSO-based adducts. The XRD
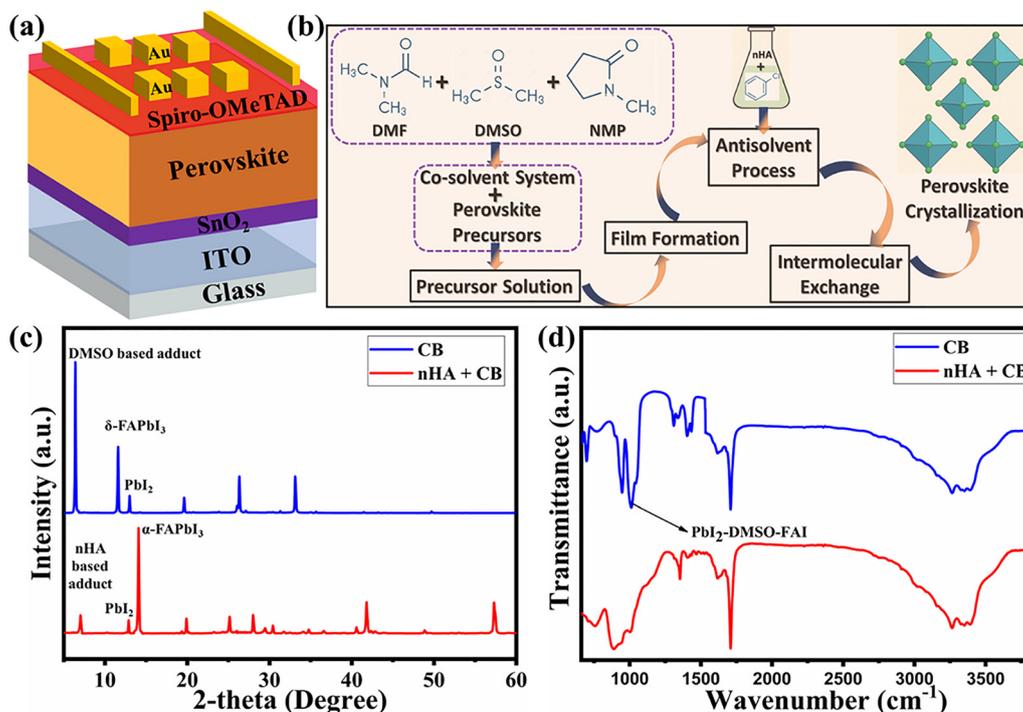

Fig. 1 (a) Device architecture. (b) Schematic of the synthetic process. (c) XRD patterns of the unannealed perovskite film. (d) FTIR spectra of the unannealed perovskite film.

pattern for the chlorobenzene-based perovskite film reveals a distinct peak corresponding to the DMSO-based adduct at a 2θ angle of 8.3°, a δ-phase peak at 11.8°, and the lead iodide (PbI_2) phase at 12.8°.[27,28] In contrast, for the n-HA with chlorobenzene-based perovskite film, the adduct peak intensity is reduced and shifts to a higher 2θ angle. This shift suggests that n-HA suppresses the formation of the DMSO-based adduct and promotes the formation of the α-phase. Notably, no δ-phase is observed in this case, although a small PbI_2 peak remains. Although direct NMR measurements were not performed in this study, amine–Pb^{2+} coordination leading to intermediate adduct formation has been unambiguously confirmed by ^{1}H NMR spectroscopy analysis of closely related perovskite systems, showing characteristic N–H signal shifts upon coordination, consistent with the interaction proposed here.[26] To further understand the mechanism and observations from the XRD analysis, the following set of equations can be written:

(1) Solvent complex formation

Solvent molecules coordinate with PbI_2 as follows:

$$PbI_2 + DMSO \rightleftharpoons PbI_2\text{–}DMSO,$$

$$PbI_2 + DMF \rightleftharpoons PbI_2\text{–}DMF.$$
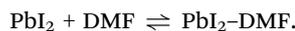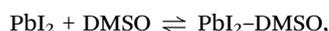
These complexes ensure proper solubility and precursor stability.

(2) Precursor solution formation

In the co-solvent system (DMF, DMSO, and NMP), the perovskite precursors form a solution as follows:

$$FAI_{(sol)} + PbI_2 + DMSO \rightleftharpoons FA^+PbI_3^-DMSO.$$

This complex represents a liquid-phase intermediate (also observed during slow evaporation), aiding uniform film formation.

(3) Upon addition of antisolvent (CB)

Antisolvent quickly extracts coordinating solvents (DMSO), initiating crystallization as follows:

$$FA^+PbI_3^-DMSO \xrightarrow{CB+annealing} FAPbI_3 + DMSO_{(out)}.$$
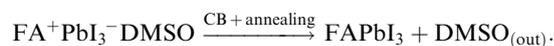
Also, the residual PbI_2 reacts directly with FAI upon DMSO removal as follows:

$$FAI + PbI_2 \xrightarrow{CB+annealing} FAPbI_3.$$
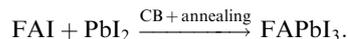
(4) Intermolecular exchange with nHA

When CB + nHA is used during the antisolvent process:

$$PbI_2 - DMSO + nHA \xrightarrow{CB} PbI_2 - nHA + DMSO_{(out)},$$

$$FAI + nHA \rightleftharpoons FA^+ + nHA^+ + I^-.$$
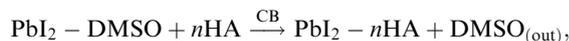
Then, the crystallization occurs *via* direct reaction as follows:

$$FA^+ + PbI_2 + I^- \xrightarrow{CB+nHA} FAPbI_3.$$
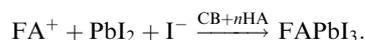
(5) Surface passivation *via* nHA coordination

Excess nHA can coordinate with surface Pb^{2+} ions, possibly due to chelation *via* the NH_2 lone pair, reducing defects as follows:

$$Pb^{2+} + nHA \rightarrow Pb\text{–}NH_2(C_7H_{15}).$$
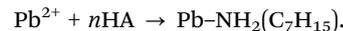
These findings indicate that nHA, when used with an antisolvent, interacts with PbI_2 and formamidinium iodide (FAI), inhibiting the formation of the FAI–DMSO–PbI_2 adduct and facilitating the formation of the photoactive α-phase without the need for annealing. This stabilization of the black phase is attributed to intermolecular substitution between n-HA and the moisture-induced DMSO-based adducts, which facilitates the crystallization of the desired perovskite phase under ambient conditions.[26] The absence of characteristic peaks related to DMSO-adducts and the emergence of new peaks associated with n-HA in the XRD pattern further confirmed this intermolecular exchange. To corroborate this, FTIR spectroscopy was performed on the unannealed perovskite films. In the pristine film, a distinct vibrational stretching peak at 1020 cm^{-1} was observed, corresponding to DMSO-adducts involving FAI and PbI_2. In contrast, this peak disappeared in the n-HA-modified film, supporting the hypothesis that n-HA disrupts DMSO-based adduct formation (Fig. 1d). Collectively, these findings validate the role of n-HA in mitigating moisture-related degradation pathways and stabilizing the photoactive black phase in air-ambient conditions.

3.2 Morphology and crystallinity improvement

Fig. 2(a)–(d) presents the cross-sectional and top-view SEM images of perovskite films fabricated with and without n-HA modification. In the pristine perovskite film, distorted grains are clearly observed, whereas the n-HA-modified film exhibits a more uniform morphology (Fig. 2a and b). The incorporation of n-HA results in a smoother and more homogeneous perovskite film compared with the control sample. Distorted grains (red circles) were observed in the pristine sample. Additionally, cross-sectional analysis reveals that the modified film is more compact and uniform than its pristine counterpart (Fig. 2c and d). The
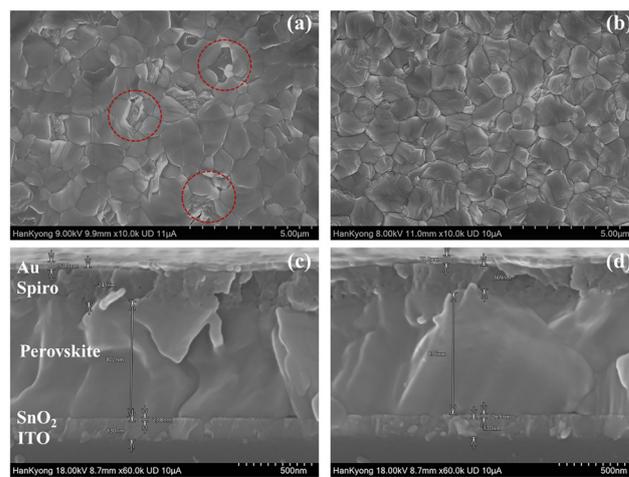

Fig. 2 (a) Top-view SEM image of the control perovskite film. (b) Top-view SEM image of the modified perovskite film. (c) Cross-sectional SEM image of the control device. (d) Cross-sectional SEM image of the modified device.

average grain size of the n-HA-modified perovskite film is significantly larger than that of the control film, indicating improved crystallization and film quality. This enhancement suggests that n-HA facilitates the growth of perovskite structures during the anti-solvent dripping and annealing processes, thereby optimizing the crystallization process. Such behavior is consistent with prior observations that medium-chain alkyl amines effectively regulate perovskite nucleation and growth without compromising carrier transport.[29,30] The AFM images in Fig. S5 further support these findings, demonstrating a reduction in root mean square (RMS) roughness from 26.35 nm to 20.95 nm after n-HA modification. The decrease in surface roughness enhances the uniformity and compactness of the perovskite film, which, in turn, improves charge transport at the interface.[31] This reduction in interfacial defects and irregularities contributes to enhanced device performance and stability. SEM and AFM analyses revealed that the incorporation of n-HA into the antisolvent process led to smoother and more uniform perovskite films with larger grain sizes and reduced grain boundaries. The improved grain quality minimized the number of defects, contributing to enhanced device performance.

Furthermore, microscopic pinholes and film non-uniformity can significantly degrade the shunt resistance (R_{SH}) of PSCs, which is a critical parameter indicating the ability of the device to suppress current leakage under open-circuit conditions.[32] The presence of non-uniformities introduces unintended pathways for charge carriers, leading to a reduction in R_{SH} and increased energy losses.[33] Additionally, pinholes and grain distortions negatively impact the FF, a key parameter influencing the PCE, by disrupting film continuity and hindering charge transport. Moreover, these factors contribute to reducing the V_{OC} by generating non-radiative recombination sites, thereby limiting the ability of the cell to sustain voltage when isolated from an external circuit. The interdependence of FF and V_{OC} with R_{SH} is quantitatively represented by the following correlations:[34–36]

$$V_{OC} = \frac{qV_{OC}}{nkT} = \ln\left\{\frac{J_{Ph}}{J_0}\left(1 - \frac{V_{OC}}{J_{Ph}R_{SH}}\right)\right\},$$

$$FF = \frac{V_{OC} - \ln(V_{OC} + 0.72)}{V_{OC} + 1}.$$

Here, n stands for the ideality factor, J_{Ph} for the photocurrent density, J_0 for the reverse saturation current, and V_{OC} for the normalised voltage under open-circuit conditions. Therefore, the R_{SH} of the devices ultimately improves when n-HA is used to improve the morphology (Fig. S6). As shown in the following section, this rise in R_{SH} immediately results in improved FF and V_{OC}, which, in turn, raises the PCE for n-HA modified devices.

Further, the impact of n-HA alteration on the crystallinity, phase purity, and crystal structure of the perovskite films was investigated using XRD analysis, as shown in Fig. 3a. Different diffraction peaks were seen in both control and n-HA-modified films, each of which corresponds to a different cubic perovskite crystal plane. In contrast, the intensities of other diffraction peaks were negligible compared with those corresponding to the (0 0 1) and (0 0 2) planes in the nHA-modified sample, indicating a preferred crystallographic orientation in the perovskite film. The enhanced strength of the distinctive characteristic diffraction peak indicates that adding n-HA improved the purity of the photoactive phase rather than altering the crystal structure of the perovskite films. In the XRD pattern of the control perovskite film, small diffraction peaks corresponding to the photo-inactive phase and residual PbI_2 were observed, indicating incomplete crystallization and suboptimal formation of the photoactive phase. In contrast, the modified film exhibited no such peaks, suggesting the suppression of undesired phases and the formation of a highly pure photoactive perovskite phase. This indicates that n-HA modification effectively enhances phase purity and promotes improved crystallization of the perovskite film. Furthermore, the reduced full width at half maximum (FWHM) of the characteristic diffraction peak compared with the control film demonstrated the improved crystallinity of the n-HA-modified film (Fig. 3b).[37] These findings suggest that n-HA plays a crucial role in refining the structural properties (i.e., crystallinity and morphology) of the perovskite layer.

3.3 Effect of n-HA modification on bonding and interactions within the perovskite film

XPS was employed to investigate the elemental states and interaction of nHA in the perovskite film. In the control sample,
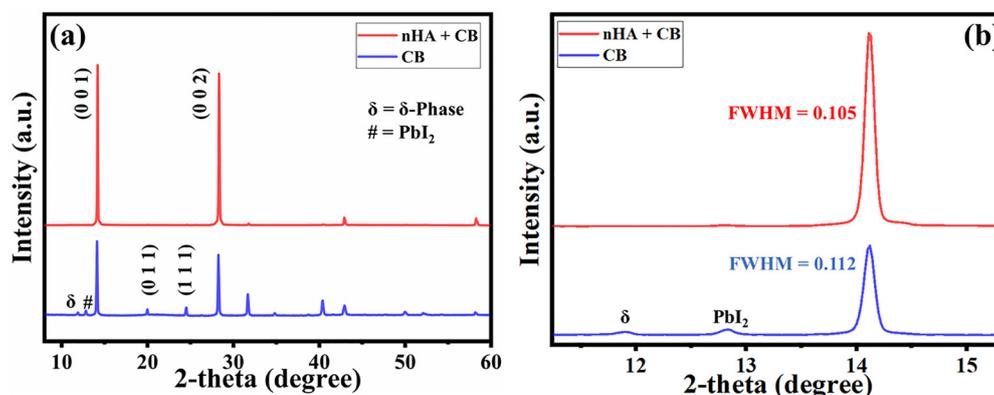

Fig. 3 (a) Comparison of the XRD patterns of the annealed–modified and control perovskite films. (b) Calculation of the FWHM for the (0 0 1) characteristic peak of the target and control perovskite films.
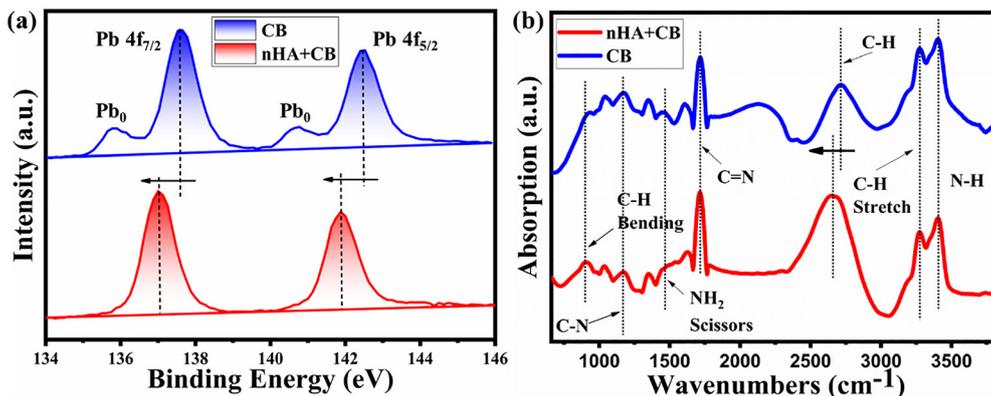
Fig. 4 (a) XPS analysis of the Pb 4f peak of pristine and modified perovskite films. (b) FTIR spectroscopic investigation of the effect of *n*HA in the perovskite film.

characteristic Pb 4f peaks were observed at 137.61 eV and 142.46 eV (Fig. 4a). Upon *n*HA modification, these peaks shifted towards lower binding energy of 137.11 eV and 141.88 eV, respectively, indicating the formation of strong interactions between Pb and *n*HA. Furthermore, the control film exhibited additional peaks at 135.83 eV and 140.74 eV, attributed to metallic Pb^0 arising from uncoordinated lead. In contrast, these Pb^0-related peaks were absent in the *n*HA-modified film, confirming the effective passivation of uncoordinated Pb metal by *n*HA. This is an effect of the interaction between the uncoordinated lead and the Lewis base group in *n*HA.[38] Furthermore, a shift in the N 1s peak towards lower binding energy was observed, indicating a strong interaction between *n*HA and the perovskite film (Fig. S7).

The FTIR analysis reveals distinct structural and chemical changes upon incorporating *n*HA (Fig. 4b). The suppression of the –NH$_2$ vibrational peak at 1448 cm^{-1} in the FTIR spectra indicates a reduction in the uncoordinated or free amine groups within the FAPbI$_3$ perovskite structure. This is a desirable effect observed when employing CB alone. The presence of uncoordinated –NH$_2$ groups typically suggests incomplete interaction between the formamidinium (FA$^+$) cations and the PbI$_6^{4-}$ octahedra, which can lead to defect formation and instability in the perovskite film. The CB + *n*HA based sample showed suppression of this peak, which implies enhanced coordination and improved crystallinity and phase purity of the FAPbI$_3$ structure. In contrast, perovskite films fabricated without the *n*HA exhibit a pronounced NH$_2$ peak, reflecting a higher concentration of residual or loosely bound FA$^+$ cations, which can act as trap states and adversely affect device performance. Simultaneously, the red shift in the C–H stretching peak of the *n*HA + CB based sample from 2717 cm^{-1} to 2658 cm^{-1} signifies enhanced molecular interactions, likely due to hydrogen bonding or changes in the local environment, which improve film crystallinity or chemical bonding with *n*HA. These spectral signatures support the chemical integration of *n*HA and confirm the modifications induced by thermal annealing in the perovskite film.

3.4 Defects and recombination loss analysis

Additionally, analysis of the dark *J–V* curves for both electron-only and entire devices was conducted to assess defect

passivation and the reduction of recombination losses. Fig. 5a shows the SCLC analysis conducted on electron-only devices utilising the configuration ITO/SnO$_2$/perovskite/LiF/Au. LiF was chosen because it can be deposited by thermal evaporation, enabling solvent-free processing that is compatible with air-ambient fabrication and prevents possible solvent-induced degradation of the perovskite layer. This study analyses the significant increase in current within the trap-filled region under elevated bias conditions. The relationship between current and voltage is linear in the ohmic region, specifically at low-bias conditions. As the bias increases into the trap-filled zone, the trap states progressively fill, ultimately achieving a saturation threshold known as the trap-filled limiting voltage (V_{TFL}). The equation presented below is utilised for calculating the trap density:[39]

$$\frac{N_t}{2} = \frac{(\varepsilon_0 \varepsilon V_{\text{TFL}})}{(eL^2)}.$$

In this equation, ε signifies the dielectric constant, ε_0 represents the vacuum permittivity, e denotes the fundamental charge, and L corresponds to the perovskite thickness. The dielectric constant is found using the following equation:

$$\varepsilon = \frac{LC_g}{A\varepsilon_0},$$

where C_g represents the geometric capacitance of the perovskite layer and A signifies the active area of the device. The geometric capacitance is associated with the electric field induced by ions, which plays a role in the hysteresis behaviour observed in PSCs, and can be evaluated using impedance analysis. This study utilised the dielectric constant value for perovskite as documented in the available literature for both control and altered devices.[40] The V_{TFL} values for the electron-only pristine and altered devices were measured at 0.68 V and 0.57 V, respectively. Considering the dielectric constant, the perovskite thickness as observed in the cross-sectional SEM image, and the measured V_{TFL}, the bulk defect density was determined to be 1.45×10^{15} cm^{-3} for the pristine devices and 9.85×10^{14} cm^{-3} for the modified devices, as illustrated in Fig. 5a. Hence, the
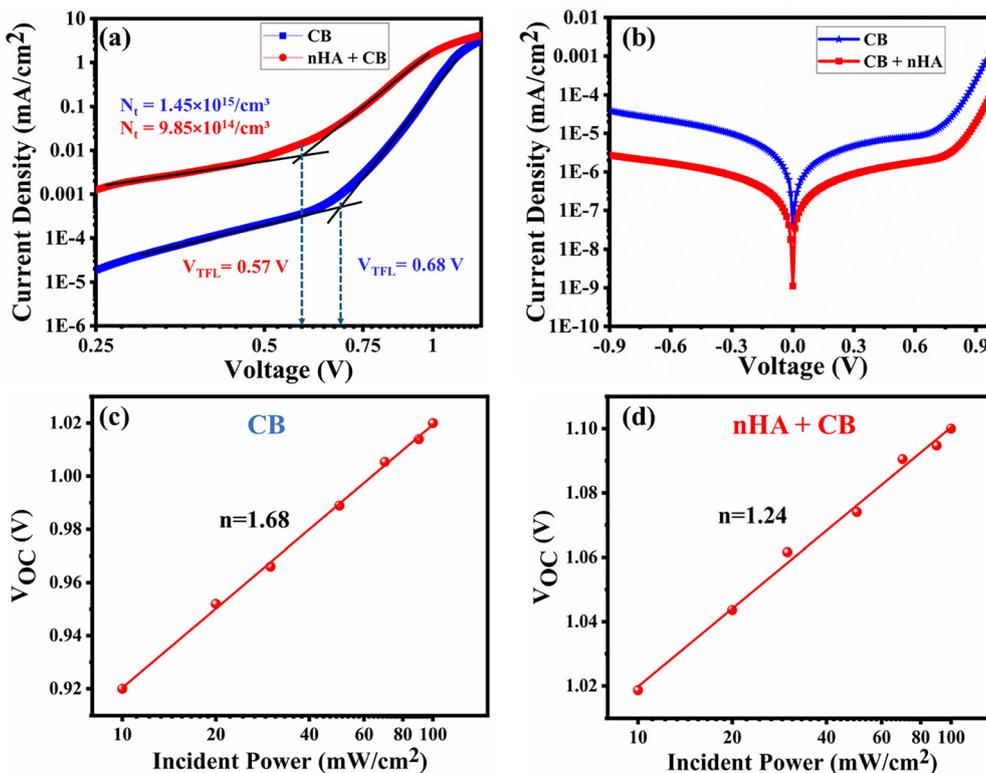
Fig. 5 Dark *JV* analysis plots of the (a) electron-only device and (b) complete device. Variation of V_{OC} with light intensity for the (c) CB-based device and (d) *n*HA + CB-based device.

implementation of anti-solvent engineering resulted in a reduction of bulk defect density within the active layer, contributing to an enhancement in the V_{OC} of the aimed device. Dark *J–V* analysis was conducted to further investigate the reduction in defects within the modified device. The modified device exhibited a reduction in dark current compared with the pristine device, indicating that the defect sites were successfully passivated with *n*-HA, resulting in decreased recombination losses (Fig. 5b).[41] The passivation resulted in improvements in J_{SC} and V_{OC} values, as demonstrated by the overall effectiveness of the device (see Section 3.6 for discussions on device performance).

A light intensity dependency study was conducted to further examine the reduced recombination losses in the device. Fig. 5c and d illustrate the relationship between the V_{OC} and varying light intensities for both the control and modified devices. This analysis demonstrates that as the ideality factor '*n*' approaches 1, it implies that there is minimal defect-generated non-radiative Shockley–Read–Hall (SRH) recombination occurring within the device. The factor *n* was calculated by analysis of the V_{OC} curve with respect to light intensity, employing the following equation:[42]

$$n = \frac{q}{K_B T} \times \frac{d(V_{OC})}{d(\ln I)}.$$

this equation, *q* signifies the fundamental charge, K_B is the Boltzmann constant, *T* refers to the temperature of the cell, and

I represents the impinging light intensity. The intensity was adjusted utilising ND (neutral density) filters, with values ranging from 10 mW cm^{-2} to 90 mW cm^{-2}, in order to assess the trap states present within the bulk material. The value of *n* for the modified device was determined to be 1.24, which is notably lower than that recorded for the pristine devices (1.68). The results demonstrate that modifications of the film can substantially decrease nonradiative recombination, which is consistent with the findings from the SCLC analysis and the dark current measurements.[18]

The series resistance (R_S) plays a crucial role in determining the overall efficiency of PSCs. High R_S results in energy losses during charge transport, limiting the fill factor (FF) and, consequently, the PCE.[43] A higher R_S can also reduce the J_{SC} by impeding charge extraction, leading to recombination losses.[44] Therefore, minimizing R_S is essential for improving the electrical performance of PSCs.[45] Fig. S8 presents the statistical distribution of the R_S for PSCs fabricated with two different processing conditions of anti-solvents. The results indicate that devices fabricated with *n*HA + CB exhibit significantly lower R_S compared with those with CB alone. The median R_S value for the CB-based devices is notably higher, with a broader spread, signifying increased charge transport resistance and variability among devices. In contrast, the *n*HA + CB based devices demonstrate a more uniform and lower R_S, suggesting improved charge transport and reduced interfacial resistance. These results suggest that incorporating *n*HA in the processing

step leads to enhanced charge extraction and reduced energy losses, which can contribute to overall device performance improvements. The observed reduction in R_S for the nHA + CB based devices aligns well with the improvements in crystallinity, grain size, and morphology, as well as the reduction in defect densities. Higher crystallinity and larger grain sizes facilitate better charge transport by minimizing resistance generated by grain boundary defects and suppressing charge carrier recombination.[16] Additionally, reduced defect density lowers non-radiative recombination centers, thereby improving charge extraction and decreasing resistive losses.

3.5 Effect on absorbance and charge dynamics

UV-Vis absorption assessments were performed to assess the impact of n-HA on the light-absorbing capabilities of the perovskite films. Under UV-visible irradiation, the perovskite film formed using n-HA modified antisolvent exhibits slightly increased light absorption compared with those deposited from unmodified antisolvent (Fig. S9 (inset)). The increased absorbance is mainly attributed to the improved crystallinity, grain size, and compactness of the perovskite films treated with n-HA.[46] The modifications affect the energy bandgap, which is a critical parameter for the efficiency of solar cells. The variation in absorption spectra resulted in a slight reduction in the bandgap of the perovskite, shifting from 1.522 eV to 1.519 eV, as demonstrated by Tauc plot analysis (Fig. S9). The improvement in the absorption and the slight modification in the bandgap can be attributed to the optimised morphology and better crystallization, as demonstrated by the SEM images.[47,48] The results demonstrate the improvement in J_{SC} of devices modified with n-HA, which is subsequently verified through J–V measurements under illumination. Furthermore, steady-state photoluminescence (SS-PL) and time-resolved photoluminescence (TR-PL) analyses were conducted to evaluate the impact of n-HA modification on charge recombination dynamics and carrier lifetimes in perovskite films deposited on glass substrates. As shown in Fig. 6a, the SS-PL intensity of the modified perovskite film was significantly higher than that of the pristine film, indicating a reduction in non-radiative

recombination of photo-generated carriers.[46] This suggests that the anti-solvent-engineering strategy effectively passivated trap states, facilitating efficient charge extraction to the transport layers and subsequently enhancing J_{SC}, as observed in the device performance section. Additionally, the TR-PL spectra were analyzed using the following double-exponential equation:

$$I(t) = I_0 + D_1 \exp\left(\frac{t}{\tau_1}\right) + D_2 \exp\left(\frac{t}{\tau_2}\right),$$

where D_1 and D_2 represent the associated decay time constants, and τ_1 and τ_2 are the decay amplitudes corresponding to the fast and slow decay processes, respectively. The average carrier lifetime (τ_{av}) was calculated using the following equation:[49,50]

$$\tau_{av} = \frac{D_1\tau_1^2 + D_2\tau_2^2}{D_1\tau_1 + D_2\tau_2}.$$

The above equation provides a weighted average lifetime, accounting for both fast and slow recombination dynamics in the perovskite film. A significant enhancement in carrier lifetime was observed following the anti-solvent modification, as illustrated in Fig. 6b. This indicates suppressed charge recombination dynamics within the perovskite film. Specifically, the weighted average carrier lifetime increased from 259.13 ns f the pristine device to 814.40 ns for the modified device (Table S1). This notable increase further confirms the improved optoelectronic quality and reduced defect density of the perovskite films processed with antisolvent engineering. These findings suggest a reduction in both non-radiative and radiative recombination events within the bulk and at the surface of the nHA-modified, highly oriented perovskite film. This improvement can be attributed to enhanced film quality and effective trap-state passivation facilitated by the nHA treatment.[51]

Furthermore, Fig. S10(a) and (b) demonstrates an elementary power-law connection involving the J_{SC} and light intensity ($J \propto I^x$) for two separate cells constructed with and without the n-HA process. The graph illustrates the logarithmic relationship between J_{SC} and intensity. The intensity dependence in a solar cell, especially one featuring an interfacial barrier or
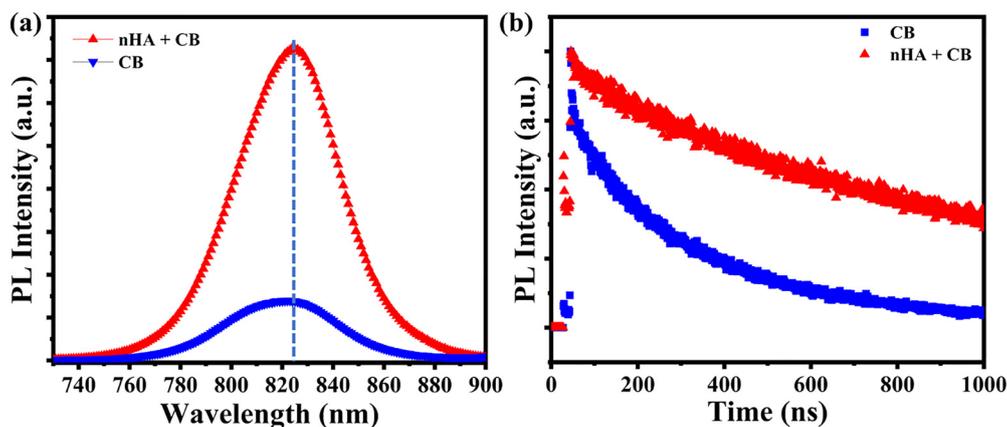

Fig. 6 (a) SS–PL plot of the control and modified perovskite films. (b) TR–PL plot of the control and modified perovskite films.

carrier imbalance, demonstrates SCL behaviour, which is characterised by a power law with $\alpha = 3/4$.[52] Devices lacking SCL effects typically exhibit α values close to 1, signifying that all the generated charge-carriers are effectively gathered by the electrodes prior to recombination. In the perovskite devices examined in this study, the measured values of α are 0.985 for the control device and 0.998 for the modified device. The values demonstrate a significant proportional relationship between the J_{SC} and incident photon, highlighting the effective response of the device to variations in light intensity. The α metrics for n-HA based device exhibit a slight improvement when compared with those of the pristine device, thereby confirming enhanced charge transport and elevated J_{SC} values. Additionally, the reduction in grain boundaries and defects associated with these boundaries, accomplished by the formation of evenly distributed perovskite grains that extend from the ETL to the HTL (as illustrated in Fig. 2c and d), is expected to mitigate recombination losses significantly.

3.6 Device performance

The photovoltaic performance of the fabricated devices was evaluated under room temperature standard test conditions using simulated sunlight. For solar cells made with and without n-HA, the performance parameters, including V_{OC}, J_{SC}, PCE, and FF, were identified and compared (Fig. 7a and b). The device employing n-HA in the antisolvent achieved a champion PCE of 22.56% in the reverse scan, with negligible hysteresis and excellent reproducibility. This PCE is the result of other parameters: a V_{OC} of 1.10 V, a J_{SC} of 25.17 mA cm^{-2}, and an FF of 81.47%. The highest performing PSC in the reverse scan for

devices not having n-HA exhibited a V_{OC} of 1.02 V, a J_{SC} of 24.58 mA cm^{-2}, and an FF of 78.79%, resulting in a PCE of 19.75%. A boost in IPCE intensity was observed within the wavelength range of 400–800 nm in the modified device compared with that of the pristine device. This improvement is due to enhanced transfer of charges and charge collection effectiveness. The integrated J_{SC} for the control and target devices measured 23.20 mA cm^{-2} and 24.33 mA cm^{-2}, respectively, which is in close agreement with the results derived from the J–V measurements (Fig. 7c and d). The proposed development strategy has notably improved the consistency and performance metrics of the ambient air-fabricated devices.

The long-term stability assessments of both targeted and pristine best-performing devices have been performed, as shown in Fig. 8a. The optimized modified device exhibited remarkable stability, maintaining an efficiency close to 90% even after 2000 hours of preservation in the dark, as measured at regular intervals. The optimized pristine devices exhibit 48.01% retention of the initial PCE. The improved stability observed in devices utilizing n-HA is due to the reduced defect levels and superior morphology of the perovskite film.[53] The stability tests showed minimal deterioration after 2000 hours under ambient conditions, demonstrating the effectiveness of n-HA in mitigating moisture-induced degradation. Although direct MPPT measurements were not conducted due to instrumental limitations, the negligible hysteresis and prolonged operational stability strongly suggest reliable maximum power operation, as commonly reported for well-passivated perovskite devices.[54,55]
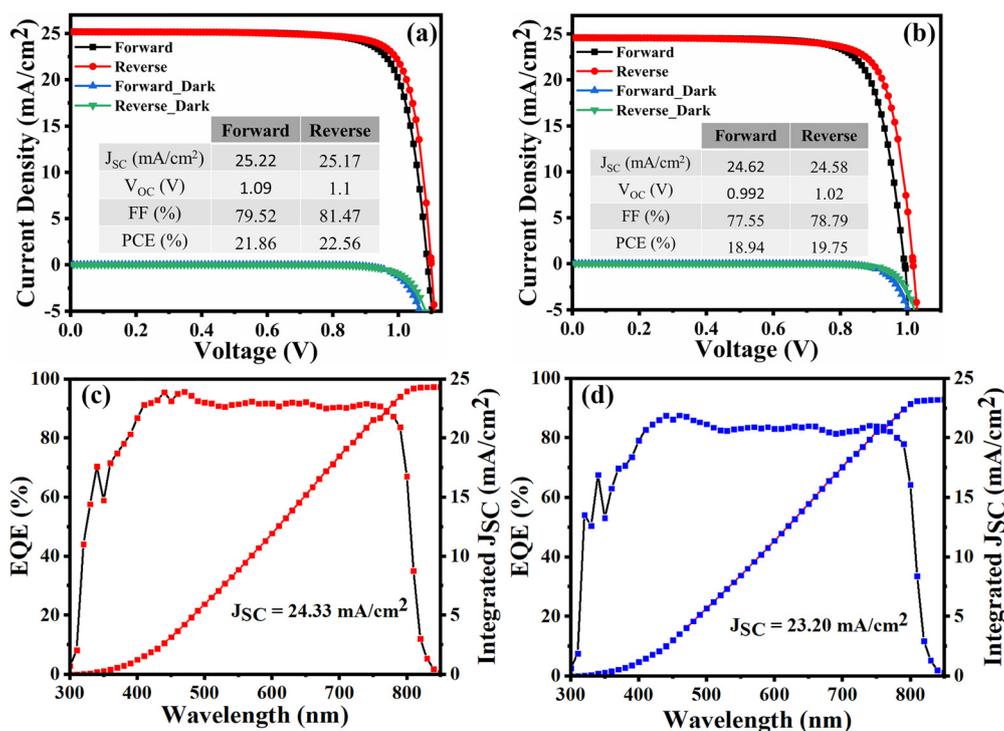

Fig. 7 JV curves of the best performing devices (a) with nHA and (b) without nHA. EQE and integrated J_{SC} analysis plots for the best performing devices (c) with nHA and (d) without nHA.
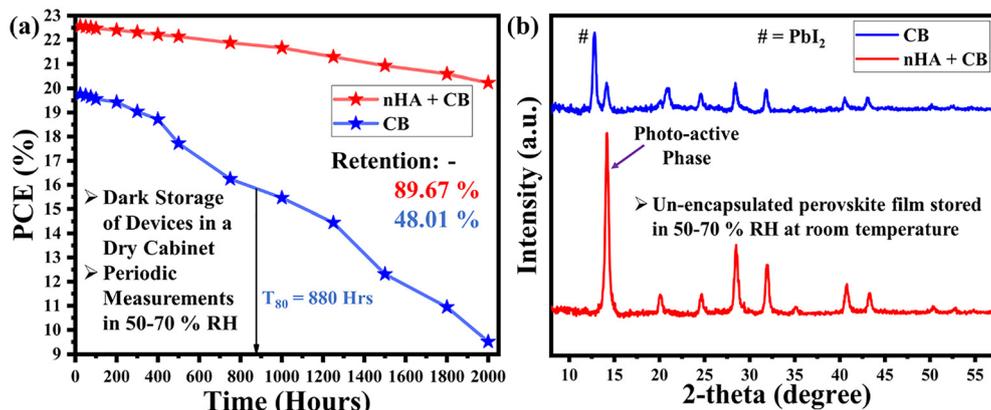
Fig. 8 (a) Long-term device stability comparison for unencapsulated devices. (b) Stability analysis of unencapsulated perovskite films stored under high humidity for three months.

Moreover, the stability of the perovskite films exposed to high-humidity conditions was evaluated using XRD analysis (Fig. 8b). Both the modified and control films were stored under ambient conditions at an RH level of 50%–70% for a prolonged duration of three months. The modified films exhibited minimal changes in physical appearance, with only a few pinholes observed. In contrast, the control films underwent a phase transition, as evidenced by the fading of the black perovskite phase and the emergence of a yellowish appearance. XRD analysis further corroborated these observations, revealing the absence of significant lead-related peaks in the modified films. Additionally, the modified films retained a strong characteristic peak corresponding to the black perovskite phase, indicating enhanced structural stability.

Further, the environmental stability of the fabricated solar cells was assessed by exposing the unencapsulated devices to an ambient environment with 60% relative humidity in the dark at room temperature. Device performance was periodically recorded, with Fig. S11 illustrating the normalized PCE over time. As anticipated, the passivated devices demonstrated significantly enhanced environmental stability compared with the control devices, highlighting the effectiveness of the modification strategy for long-term stability. The control device had a T_{80} lifespan of 87 hours, whereas the modified device had a substantially longer T_{80} lifetime of 316 hours, with better PCE retention over 500 hours. The superior stability of the passivated devices, compared with the control device, can be attributed to the formation of secondary bonds and a more hydrophobic surface.[56] These factors collectively enhance resistance to environmental degradation, ensuring sustained device performance over an extended period. Moreover, as anticipated, the modified devices also demonstrated significantly enhanced thermal stability, further reinforcing the effectiveness of the modification strategy toward stressed thermal conditions. To evaluate thermal stability, the devices were heated at 65 °C, and their performance was periodically recorded. The pristine device exhibited a T_{80} lifetime of 107 hours, whereas the modified device demonstrated a significantly extended T_{80} lifetime of 259 hours, with greater retention of PCE over a period of 500 hours (Fig. S12). This enhanced thermal stability can be attributed to the passivated surface and improved perovskite morphology, which effectively mitigates phase segregation under thermal stress.[57]

To evaluate the repeatability and reproducibility of the devices, we have produced more than 100 devices for each pristine and n-HA modified batch (Fig. S13). Every performance metric was compared using a distribution plot. The data indicate that the n-HA guided fabrication method resulted in improved average device functionality metrics. The target device, designed according to the optimal concentration of n-HA, exhibited an average J_{SC} of 25.07 $\pm$ 0.80 mA cm^{-2}, an average V_{OC} of 1.07 $\pm$ 0.04 V, an average FF of 79.54% $\pm$ 2.99%, and an average PCE of 20.94% $\pm$ 1.56%. The pristine device exhibited an average J_{SC} of 22.78 $\pm$ 2.18 mA cm^{-2}, an average V_{OC} of 0.98 $\pm$ 0.06 V, an average FF of 73.15% $\pm$ 5.76%, and an average PCE of 17.11% $\pm$ 2.64%. The altered device exhibited a reduced hysteresis effect along with an improved V_{OC}. This is an artifact of impeded halide migration and halide vacancy passivation by the Lewis functional group of n-HA.[58] Post antisolvent engineering, a clear improvement in all photovoltaic parameters was observed. The enhancement in perovskite film quality results from an increase in grain size, and improved crystallinity is the prime factor for heightened performance. The identified factors contributed to enhanced photoabsorbance, passivated grain boundaries, and decreased series resistance, which subsequently led to a reduction in nonradiative recombination losses.

4. Conclusion

We have demonstrated an effective antisolvent engineering strategy to stabilize the photoactive α-FAPb(I$_x$Br$_{1-x}$)$_3$ phase using n-HA. n-HA helped in the intermediate phase modulation by replacing the moisture-induced detrimental compounds. The incorporation of n-HA during the film formation process not only stabilizes the perovskite phase under ambient conditions but also enhances film morphology and device performance. The Lewis base group in n-HA passivates the metallic

lead appropriately, and its hydrophobic nature mitigates the early degradation due to moisture. This approach achieves a remarkable PCE of 22.56%, with minimal hysteresis and excellent long-term stability. Further, the passivated perovskite film-based devices showed better performance retention under stressed conditions. Our findings highlight the potential of antisolvent engineering for the intermediate phase modulation and fabrication of high-performance PSCs in air-ambient environments.

Conflicts of interest

The authors declare no conflicts of interest.

Data availability

Supplementary information is available. See DOI: https://doi.org/10.1039/d5ya00348b.

The data supporting this article have been included as part of the supplementary information and any additional required data will be available upon request from the corresponding author.

Acknowledgements

References

1 Q. Jiang and K. Zhu, *Nat. Rev. Mater.*, 2024, **9**, 399–419.

2 https://www.acap.org.au/post/world-leading-27-perovskite-efficiency-record-achieved-by-unsw-and-soochow-university-with-acap-su.

3 Z. Huang, Y. Bai, X. Huang, J. Li, Y. Wu, Y. Chen, K. Li, X. Niu, N. Li, G. Liu, Y. Zhang, H. Zai, Q. Chen, T. Lei, L. Wang and H. Zhou, *Nature*, 2023, **623**, 531–537.

4 Y. Zhang, A. Kirs, F. Ambroz, C.-T. Lin, A. S. R. Bati, I. P. Parkin, J. G. Shapter, M. Batmunkh and T. J. Macdonald, *Small Methods*, 2021, **5**, 2000744.

5 H. Kim, M. Hashimoto, Y. Ohkura, T. Ito, H. Takahashi, H. Sato, J. Kim, N. Shibayama, T. Miyasaka and G. M. Kim, *Chem. Eng. J.*, 2025, **505**, 159571.

6 N. K. Bansal, S. Porwal, G.-M. Kim and T. Singh, *Chem. Eng. J.*, 2025, 165149, DOI: 10.1016/j.cej.2025.165149.

7 C. Yang, W. Hu, J. Liu, C. Han, Q. Gao, A. Mei, Y. Zhou, F. Guo and H. Han, *Light: Sci. Appl.*, 2024, **13**, 227.

8 S. Lee and H. S. Jung, *Korean J. Chem. Eng.*, 2024, **41**, 3703–3715.

9 F. Wang, Z. Ye, H. Sarvari, S. M. Park, A. Abtahi, K. Graham, Y. Zhao, Y. Wang, Z. D. Chen and S. Li, *J. Power Sources*, 2019, **412**, 359–365.

10 J. Han, K. Park, S. Tan, Y. Vaynzof, J. Xue, E. W.-G. Diau, M. G. Bawendi, J.-W. Lee and I. Jeon, *Nat. Rev. Methods Primers*, 2025, **5**, 3.

11 Y. Zhang, X. Sun, Q. Wang, Y. Yue, Z. Guan, H. Liu, Z. Li, Y. Zhang, M. Qiu, D. Li, F. Liu, J. Wei and H. Li, *Adv. Energy Mater.*, 2025, **15**(27), 2500156.

12 W. Fan, K. Deng, Y. Shen, Y. Bai and L. Li, *Angew. Chem., Int. Ed.*, 2022, **61**(42), e202211259.

13 A. Mallick and I. Visoly-Fisher, *Mater. Adv.*, 2021, **2**, 6125–6135.

14 Y. Zhao, W. Zhou, Z. Han, D. Yu and Q. Zhao, *Phys. Chem. Chem. Phys.*, 2021, **23**, 94–106.

15 M. Li, R. Sun, J. Chang, J. Dong, Q. Tian, H. Wang, Z. Li, P. Yang, H. Shi, C. Yang, Z. Wu, R. Li, Y. Yang, A. Wang, S. Zhang, F. Wang, W. Huang and T. Qin, *Nat. Commun.*, 2023, **14**, 573.

16 N. K. Bansal, S. Porwal and T. Singh, *Surf. Interfaces*, 2024, **44**, 103738.

17 S. Porwal, N. K. Bansal, S. Ghosh and T. Singh, *Energy Adv.*, 2024, **3**, 894–903.

18 Z. Dai, Y. Yang, X. Huang, S. Wan, L. Yuan, H. Wei, S. Nie, Z. Liu, Y. Wu, R. Chen and H. Wang, *Nano Energy*, 2024, **131**, 110190.

19 S. Ghosh, B. Boro, S. Porwal, S. Mishra and T. Singh, *Energy Adv.*, 2023, **2**, 1155–1165.

20 K. Zhang, X. Zhang, K. G. Brooks, B. Ding, S. Kinge, Y. Ding, S. Dai and M. K. Nazeeruddin, *Sol. RRL*, 2023, **7**, 2300115.

21 L. Chao, Y. Xia, B. Li, G. Xing, Y. Chen and W. Huang, *Chem*, 2019, **5**, 995–1006.

22 C. Chen, Y. Jiang, Y. Feng, Z. Li, N. Cao, G. Zhou, J.-M. Liu, K. Kempa, S.-P. Feng and J. Gao, *Mater. Today Phys.*, 2021, **21**, 100565.

23 S. Paek, P. Schouwink, E. N. Athanasopoulou, K. T. Cho, G. Grancini, Y. Lee, Y. Zhang, F. Stellacci, M. K. Nazeeruddin and P. Gao, *Chem. Mater.*, 2017, **29**, 3490–3498.

24 S. Ghosh, S. Mishra and T. Singh, *Adv. Mater. Interfaces*, 2020, **7**, 2000950.

25 N. K. Bansal, S. Ghosh, S. Porwal and T. Singh, *J. Mater. Sci.: Mater. Electron.*, 2023, **35**, 1.

26 M. Wang, H. Sun, L. Meng, M. Wang and L. Li, *Adv. Mater.*, 2022, **34**, 2200041.

27 F. Yang, L. Dong, D. Jang, K. C. Tam, K. Zhang, N. Li, F. Guo, C. Li, C. Arrive, M. Bertrand, C. J. Brabec and H.-J. Egelhaaf, *Adv. Energy Mater.*, 2020, **10**, 2001869.

28 M. Wang, F. Cao, K. Deng and L. Li, *Nano Energy*, 2019, **63**, 103867.

29 H. Nagasaka, M. Yoshizawa-Fujita, Y. Takeoka and M. Rikukawa, *ACS Omega*, 2018, **3**, 18925–18929.

30 Y. Tezuka, K. Umemoto, M. Takeda, Y. Takahashi, H. Ebe, J. Enomoto, S. Rodbuntum, T. Nohara, D. Fontecha,

S. Asakura, T. Chiba, M. I. Furis, T. Yoshida, H. Uji-i and A. Masuhara, *Jpn. J. Appl. Phys.*, 2020, **59**, SDDC04.

31 D. Lin, J. Fang, S. Li, Z. Zhan, H. Li, X. Wang, G. Xie, D. Wang, N. Huang, H. Peng, W. Xie, L. K. Ono, Y. Qi and L. Qiu, *Adv. Sci.*, 2025, **12**, 2407380.

32 H. Lu, Y. Liu, P. Ahlawat, A. Mishra, W. R. Tress, F. T. Eickemeyer, Y. Yang, F. Fu, Z. Wang, C. E. Avalos, B. I. Carlsen, A. Agarwalla, X. Zhang, X. Li, Y. Zhan, S. M. Zakeeruddin, L. Emsley, U. Rothlisberger, L. Zheng, A. Hagfeldt and M. Grätzel, *Science*, 2020, **370**, eabb8985.

33 R. H. Sardar, A. Bera, S. Chattopadhyay, S. I. Ali, S. Pramanik and A. C. Mandal, *Opt. Mater.*, 2024, **155**, 115818.

34 Y. Li, B. Ding, Q.-Q. Chu, G.-J. Yang, M. Wang, C.-X. Li and C.-J. Li, *Sci. Rep.*, 2017, **7**, 46141.

35 D. Grabowski, Z. Liu, G. Schöpe, U. Rau and T. Kirchartz, *Sol. RRL*, 2022, **6**, 2200507.

36 M. A. Green, *Solid-State Electron.*, 1981, **24**, 788–789.

37 Y. Liu, L. Zheng, K. Zhang, K. Xu, W. Xie, J. Zhang, Y. Tian, T. Liu, H. Xu, R. Ma, W. Huang, J. Chen, J. Bao, C. Chen, Y. Zhou, X. Wang, J. Chen and J. Wang, *J. Energy Chem.*, 2024, **93**, 1–7.

38 S. Porwal, N. K. Bansal, G.-M. Kim and T. Singh, *Small*, 2024, **20**, 2408168.

39 F. Wu, S. Mabrouk, M. Han, Y. Tong, T. Zhang, Y. Zhang, R. S. Bobba and Q. Qiao, *J. Energy Chem.*, 2023, **76**, 414–420.

40 C. Ma, B. Kim, D.-H. Kang, S.-W. Kim and N.-G. Park, *ACS Energy Lett.*, 2021, **6**, 2817–2824.

41 K. Cao, Y. Cheng, W. Zuo, B. Cai, Y. Wu, J. Zhu, Y. Zhu, H. Ning, Y. Shen, W. Shen, L. Liu and S. Chen, *J. Power Sources*, 2023, **558**, 232595.

42 P. Yang, J. Wu, J. Yang, C. Ke, W. Lin, Y. Huang, J. Tian, Y. Wang, W. Sun, Z. Lan and J. Lin, *Surf. Interfaces*, 2024, **44**, 103700.

43 N. Mundhaas, Z. J. Yu, K. A. Bush, H.-P. Wang, J. Häusele, S. Kavadiya, M. D. McGehee and Z. C. Holman, *Sol. RRL*, 2019, **3**, 1800378.

44 C. Shen, X. Ling, Y. Li, S. Chen and Y. Deng, *Appl. Phys. Lett.*, 2023, **123**(15), 153301.

45 N. K. Bansal, S. Porwal, H. Dixit, D. Kumar and T. Singh, *Energy Technol.*, 2023, **11**, 2201395.

46 X. Xu, Y. Sun, D. He, Z. Liang, G. Liu, S. Xu, Z. Li, L. Zhu and X. Pan, *J. Mater. Chem. C*, 2021, **9**, 208–213.

47 H. Hu, X. Zhou, J. Chen, D. Wang, D. Li, Y. Huang, L. Zhang, Y. Peng, F. Wang, J. Huang, N. Chen, L. Sun, X. Liu, X. Wang, J. Ouyang and B. Xu, *Energy Environ. Mater.*, 2023, **6**, e12322.

48 M. Z. Tun, P. Pansa-Ngat, P. Ruankham, K. K. Shin Thant, S. Kamnoedmanee, C. Seriwattanachai, W. Rueangsawang, R. Supruangnet, H. Nakajima and P. Kanjanaboos, *Sci. Rep.*, 2023, **13**, 2965.

49 G. Tong, L. K. Ono, Y. Liu, H. Zhang, T. Bu and Y. Qi, *Nano-Micro Lett.*, 2021, **13**, 155.

50 G. Tong, J. Zhang, T. Bu, L. K. Ono, C. Zhang, Y. Liu, C. Ding, T. Wu, S. Mariotti, S. Kazaoui and Y. Qi, *Adv. Energy Mater.*, 2023, **13**, 2300153.

51 Y. Yang, Y. Wang, Z. Qu, K. Zhang, T. Liang, S. Chen, W. Lv, F. Min, Y. Chen, Y. Qiao and Y. Song, *Angew. Chem., Int. Ed.*, 2023, **62**, e202300971.

52 T. Singh and T. Miyasaka, *Adv. Energy Mater.*, 2018, **8**, 1700677.

53 Z. Zhu, B. Ke, K. Sun, C. Jin, Z. Song, R. Jiang, J. Li, S. Kong, C. Liu, S. Bai, S. He, Z. Ge, F. Huang, Y.-B. Cheng and T. Bu, *Energy Environ. Sci.*, 2025, **18**, 4120–4129.

54 M. Saliba, T. Matsui, J.-Y. Seo, K. Domanski, J.-P. Correa-Baena, M. K. Nazeeruddin, S. M. Zakeeruddin, W. Tress, A. Abate, A. Hagfeldt and M. Grätzel, *Energy Environ. Sci.*, 2016, **9**, 1989–1997.

55 W. Tress, N. Marinova, T. Moehl, S. M. Zakeeruddin, M. K. Nazeeruddin and M. Grätzel, *Energy Environ. Sci.*, 2015, **8**, 995–1004.

56 W.-Q. Wu, Z. Yang, P. N. Rudd, Y. Shao, X. Dai, H. Wei, J. Zhao, Y. Fang, Q. Wang, Y. Liu, Y. Deng, X. Xiao, Y. Feng and J. Huang, *Sci. Adv.*, 2019, **5**, eaav8925.

57 Y. Lao, Y. Zhang, S. Yang, Z. Zhang, W. Yu, B. Qu, L. Xiao and Z. Chen, *ACS Appl. Mater. Interfaces*, 2022, **14**, 27427–27434.

58 R. J. E. Westbrook, T. J. Macdonald, W. Xu, L. Lanzetta, J. M. Marin-Beloqui, T. M. Clarke and S. A. Haque, *J. Am. Chem. Soc.*, 2021, **143**, 12230–12243.